A&A, 705, A178 (2026)
https://doi.org/10.1051/0004-6361/202557420

Astronomy & Astrophysics

The origin of B-type runaway stars based on kinematics

Yanjun Guo[1,2,★], Chao Liu[3], ZhiCun Liu[4], Chunyan Li[5], Qida Li[6], Kun Chen[1,2],
Zhanwen Han[1,2], and XueFei Chen[1,2,★]

[1] Yunnan observatories, Chinese Academy of Sciences, P.O. Box 110, Kunming 650011, China
[2] International Centre of Supernovae, Yunnan Key Laboratory, Kunming 650216, China
[3] CAS Key Laboratory of Optical Astronomy, National Astronomical Observatories, Chinese Academy of Sciences, Beijing 100101, People's Republic of China
[4] Department of Physics, Hebei Normal University, Shijiazhuang 050024, People's Republic of China
[5] Shanghai NanHui High School, Shanghai 200135, People's Republic of China
[6] Department of Astronomy, China West Normal University, Nanchong 637002, People's Republic of China

Received 26 September 2025 / Accepted 20 November 2025

ABSTRACT

Context. Runaway stars depart their birthplaces with high peculiar velocities. Two mechanisms are commonly invoked to explain their origin, the binary supernova scenario and the dynamical ejection scenario. Investigating the kinematic properties of runaway stars is key to understanding their origins.
Aims. We investigated the origins of 39 B-type runaway stars from LAMOST using orbital traceback analysis.
Methods. From the LAMOST catalog, we selected 39 B-type runaway stars and determined their spectral subtypes from key absorption lines. We then derived atmospheric parameters for each star using the Stellar Label Machine, which is trained on TLUSTY synthetic spectra computed under the nonlocal thermodynamic equilibrium assumption. Using the derived atmospheric parameters as input, we estimated stellar masses and ages with a machine learning model trained on PARSEC evolutionary tracks. We finally performed orbital traceback with `GALPY` to analyze their origins.
Results. Through orbital traceback, we find that 29 stars have trajectories entirely within the Galactic disk, whereas 10 are disk-passing yet still trace back to the disk. Two stars have trajectories that intersect those of known clusters. Their orbits show similar morphologies in both the $X-Y$ and $R-Z$ planes, and their [M/H] values are comparable, suggesting possible cluster origins. However, definitive confirmation will require additional evidence. In addition, the $V_{\rm Sp} - \upsilon \sin i$ plane shows that runaway stars with low peculiar space velocities but high $\upsilon \sin i$ remain on the Galactic disk, whereas those with high peculiar space velocities but low $\upsilon \sin i$ pass through the disk, possibly reflecting two distinct origins.

Key words. methods: data analysis – methods: statistical – catalogs – surveys – stars: early-type – stars: kinematics and dynamics

1. Introduction

Runaway stars rapidly depart from their natal clusters or associations, typically exhibiting peculiar velocities of about 30–40 km $^{-1}$ (Blaauw & Morgan 1954; Gies & Bolton 1986; Hoogerwerf et al. 2000). Most observed runaway stars are massive early-type stars, with over 30% of O stars and approximately 5−10% of B stars considered to be runaways (Blaauw 1961; Stone 1979; Mdzinarishvili & Chargeishvili 2005; Carretero-Castrillo et al. 2023). While most runaway studies have focused on OB stars, cooler runaway stars such as A/F-type candidates have also been reported in the Milky Way and in the 30 Doradus region of the Large Magellanic Cloud (Maíz Apellániz et al. 2018; Teklehaimanot & Gebrehiwot 2024). Furthermore, more than half of the known massive runaway stars exhibit high surface helium abundances and rapid rotation (Cassinelli & Churchwell 1993; Hoogerwerf et al. 2000).

Two formation scenarios have been proposed to explain their origin. One is the binary supernova scenario (BSS), first proposed by Zwicky (1957) and later developed by Blaauw (1961), in which the more massive component of a binary first undergoes core collapse, leaving behind a compact object (a neutron star or black hole). If the supernova ejects more than half of the system's total mass or imparts a significant natal kick to the remnant, the surviving companion is likely to become a runaway star (Renzo et al. 2019). Otherwise, if the system remains bound, the companion and compact object can form a runaway binary that is potentially observable as a high-mass X-ray binary (van den Heuvel et al. 2000). The other channel is the dynamical ejection scenario (DES; Poveda et al. 1967), in which early-type runaway stars are ejected from dense clusters or associations through gravitational interactions. Regarding the ejection mechanisms, binary–binary interactions are more efficient than binary–single star encounters (Hoffer 1983). Both the BSS and the DES are believed to occur, but their relative efficiencies have been debated for the past few decades (Sana et al. 2022; Chen et al. 2025).

Runaway stars formed via the DES and BSS can be distinguished in several ways. One common method for identifying runaway stars originating from the DES involves tracing back the kinematic trajectories of the stars to their parent clusters (Blaauw & Morgan 1954; Gies & Bolton 1986; Hoogerwerf et al. 2001). The chemical composition also provides valuable information. Although runaway stars from both formation scenarios typically retain their initial chemi-

---

[★] Corresponding authors: `guoyanjun@ynao.ac.cn`; `cxf@ynao.ac.cn`

cal abundances (McEvoy et al. 2017), supernova explosions in binary systems can result in α element enrichment in ejected stars (Przybilla et al. 2008; Irrgang et al. 2010). In addition, DES runaways typically have higher space velocities than BSS ones, while runaways with high $v \sin i$ are thought to arise mainly from the BSS (Sana et al. 2022).

The recent availability of extensive spectroscopic data from the Large Sky Area Multi-Object Fiber Spectroscopic Telescope (LAMOST) has provided an opportunity to investigate the origin of runaway stars (Cui et al. 2012; Zhao et al. 2012; Deng et al. 2012; Liu et al. 2020). Guo et al. (2024) identified 547 runaway stars from LAMOST Data Release 8 (DR8) and analyzed their statistical properties. Based on that catalog, Chen et al. (2025) investigated their binary fractions and evaluated the relative contributions of the BSS and DES formation scenarios. In this work we performed orbital traceback analysis for 39 B-type runaway stars from the sample identified by Guo et al. (2024) to investigate their origins.

The structure of this paper is as follows. We introduce the LAMOST data in Sect. 2. Section 3 presents the subclassification of the sample and the methods used to estimate its atmospheric and fundamental parameters Kinematic analyses and the corresponding results are presented in Sect. 4. Finally, our conclusions are summarized in Sect. 5.

2. Data

LAMOST is a 4-meter quasi-meridian reflecting Schmidt telescope located at the Xinglong station of the National Astronomical Observatories, China. The focal plane of the telescope offers a 5-degree field of view and can accommodate up to 4000 fibers (Cui et al. 2012; Zhao et al. 2012; Deng et al. 2012). Since 2012, LAMOST has conducted a Low-Resolution Spectroscopic (LRS) survey with a resolving power of $R \sim 1800$ and a wavelength coverage of 3690 ~ 9100 Å (Deng et al. 2012). In October 2018, LAMOST began a five-year Medium-Resolution Spectroscopic (MRS) survey aimed at conducting time-domain observations of objects in the Galactic region. The MRS spectra are captured with blue and red cameras, covering wavelength ranges of 4950 ~ 5350 Å and 6300 ~ 6800 Å, respectively (Liu et al. 2020).

By combining LAMOST DR8 radial velocities with *Gaia* DR3 astrometry, Guo et al. (2024) determined the peculiar tangential, radial, and space velocities of 4432 early-type stars. Following the approach of Berger & Gies (2001) and Wang et al. (2022), we identified 229 runaway stars with peculiar space velocities exceeding 43 $\mathrm{km\,s^{-1}}$, corresponding to approximately 1% of the peak of the fitted Maxwellian distribution of the space velocities. In addition, 480 further runaway candidates were selected based on their peculiar tangential velocities exceeding 33 $\mathrm{km\,s^{-1}}$, corresponding to approximately 1% of the peak of the fitted Maxwellian distribution of the tangential velocities. Because 162 sources are common to both subsamples, the final catalog comprises 547 runaway stars.

From this catalog, we selected 46 B-type runaway stars and determined their kinematic origins using orbital traceback. Although many studies restrict the definition of B stars to the B3–B9 range, we adopted the broader B0V–B9V range since our sample also includes three B2-type stars. The *Gaia* DR3 parallaxes as a function of G magnitude for the 46 runaway stars are shown in Fig. 1. Most objects are concentrated between $G = 10$ and 13 mag. Only four stars have $G < 10$ mag, two of which are at $G = 9.94$ mag, while the other two are somewhat brighter ($G = 9.3$ and $G = 8.9$ mag). In general, the magnitude distribution of our sample is nearly homogeneous.

We note that some objects within the OB temperature range could, in principle, be contaminated by blue horizontal branch (BHB) stars since the two populations exhibit similar surface gravities (Xue et al. 2008; Catelan 2009; Salgado et al. 2013; Guo et al. 2025). To assess this, we cross-matched our sample with the LAMOST BHB catalog (Vickers et al. 2021; Ju et al. 2024) and several other major BHB catalogs (Beers et al. 2007; Xue et al. 2008; Brown et al. 2008; Culpan et al. 2021), and found one overlapping source. This star has been removed from the final sample to avoid potential contamination, leaving 45 stars for further analysis.

3. Method

3.1. Spectral classification

To obtain more precise atmospheric parameters, we cross-matched the 547 early-type star candidates with the LAMOST LRS DR10 and identified 123 matches. Because our analysis focuses on B-type runaway stars, we performed spectral subclassification of these spectra through visual inspection, following the MKCLASS-based criteria established for LAMOST OB stars by Liu et al. (2019, see their Table 2).

The classification criteria are summarized as follows: For B-type stars, the strengths of hydrogen Balmer lines (such as H_δ and H_γ) increase from spectral types B0 to B9. The neutral helium lines (He I 4026, 4121, 4471, and 4713 Å) first strengthen and then weaken, reaching a maximum intensity at B2 V. In contrast, the high-excitation Mg II 4481 Å line gradually strengthens throughout the B-type sequence. When this trend is not clearly visible, we also relied on specific absorption lines and line ratios as auxiliary criteria. For stars of types B2 to B9, the ratio of He I 4471 to Mg II 4481 generally decreases (Gray & Corbally 2009; Liu et al. 2019). Furthermore, for stars of the same spectral type, the strengths of the hydrogen Balmer lines generally decrease with luminosity from the main sequence to supergiants.

Based on these classification criteria and the LAMOST-LRS spectra[1] from the LAMOST archive, we determined the spectral types for 45 B-type runaway stars, which are listed in Col. 9 of Table A.1. Figure 2 shows the spectra of five representative B-type stars (B3–B9) in the wavelength range of 3900–4750 Å, with some important spectral feature lines marked.

3.2. Atmospheric parameters

With the spectral subtypes established above, we derived atmospheric parameters for our B-type runaway stars, including effective temperature (T_{eff}), surface gravity ($\log g$), metallicity ([M/H]), and rotational velocity ($v \sin i$), using the Stellar Label Machine (SLAM; Guo et al. 2021), a data-driven forward spectral model based on support vector regression (Zhang et al. 2020). It utilizes a training dataset constructed from TLUSTY synthetic spectra derived based on nonlocal thermodynamic equilibrium (NLTE) assumption (Zhang et al. 2020). The low-resolution spectra from LAMOST offered broad wavelength coverage, enabling better constraints to be placed on T_{eff}, $\log g$, and [M/H]. On the other hand, medium-resolution spectra (MRS) provided superior rotational velocity ($v \sin i$) estimations due to higher resolution and detailed line pro-

---

[1] We used the python package `laspec` from `https://github.com/hypergravity/laspec` to normalize the spectra using a spline fit.

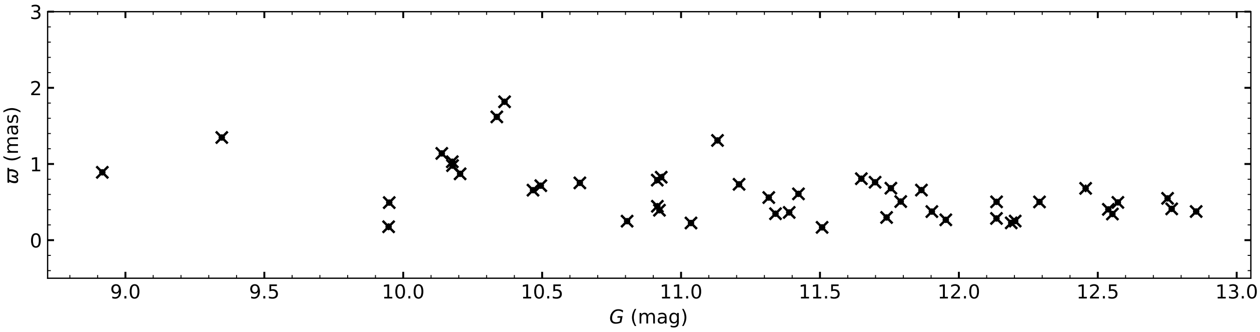

Fig. 1. *Gaia* DR3 parallaxes as a function of G magnitude. The error bars represent the parallax uncertainties.

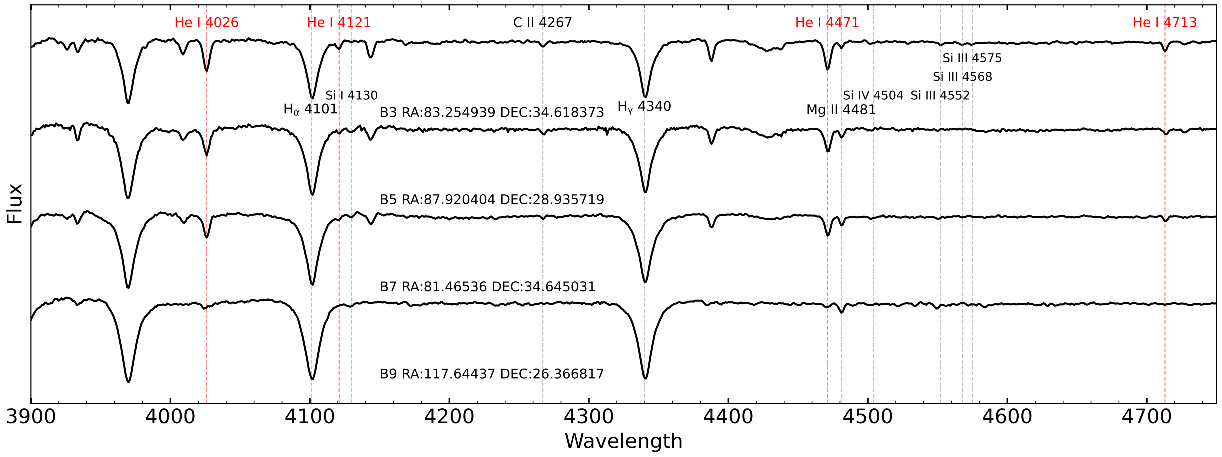

Fig. 2. Sample spectra spanning B3, B5, B7, and B9 subtypes, arranged from top to bottom. The key spectral lines He I 4026, 4121, 4471, 4713, H_δ 4101, H_γ 4340, and Mg II 4481 are labeled to highlight their variations across different subtypes. The RA and Dec of each target are listed below the corresponding spectrum.

files (Guo et al. 2021). Therefore, the values of $T_{\rm eff}$, $\log g$, and [M/H] were derived from LRS spectra, while $v \sin i$ was calculated from MRS spectra. The typical uncertainties for LAMOST MRS are $\sigma(T_{\rm eff}) = 2185$ K, $\sigma(V \sin i) = 11$ Km s^{-1} and $\sigma(\log g) = 0.29$ cm s^{-2}, while for LAMOST LRS are $\sigma(T_{\rm eff}) = 1,642$ K, $\sigma(V \sin i) = 42$ Km s^{-1} and $\sigma(\log g) = 0.25$ cm s^{-2} (Guo et al. 2021). We omitted the broad diffuse interstellar bands of 4430, 5780, 6196, 6283, and 6614 Å (Herbig 1995; Guo et al. 2021). We provide two examples from our sample, illustrating the observed spectra (black lines) along with the corresponding best-fitting spectra (dashed red lines) derived using SLAM.

However, because the NLTE TLUSTY grid has a lower temperature bound of 15 000 K, using SLAM below this limit would involve extrapolation, which can introduce biases. In contrast, Xiang et al. (2022) provide local thermodynamic equilibrium atmospheric parameters based on ATLAS12 over 7500–60 000 K, so the 9000–15 000 K regime of our sample lies within their trained range, making those estimates more reliable (i.e., interpolation rather than extrapolation). Although NLTE effects are significant for early-type stars (Lanz & Hubeny 2007), an analysis of LAMOST LRS spectra by Xiang et al. (2022) shows that, for temperatures below 25 000 K, local thermodynamic equilibrium and NLTE determinations are in good agreement. Accordingly, for stars in our sample with $T_{\rm eff} \geq 15\,000$ K, atmospheric parameters were derived using SLAM, while for those with $T_{\rm eff} < 15\,000$ K, we adopted the parameters provided by Xiang et al. (2022). The derived atmospheric parameters are listed in Table A.1.

3.3. Physical parameters

Using the atmospheric parameters obtained above, we derived the fundamental parameters, including masses and ages, for our sample following the method described by Li et al. (2025). This method employs a machine learning model implemented as a random-forest (RF) regression algorithm, which iteratively predicts stellar luminosity, mass and age based on atmospheric parameters. RF regression is an ensemble method that pools the outputs of thousands of decision trees, each grown on a random subset of the training sample, to yield a single, robust prediction. When the atmospheric parameters are fed in, every decision tree makes its own prediction, and the RF then averages them to obtain the final value. This averaging dampens the idiosyncrasies of single trees, cutting variance and yielding stable, accurate results even when the underlying relations are noisy or highly nonlinear (Li et al. 2025).

We used main-sequence stars extracted from the PARSEC 1.2S (Bressan et al. 2012; Chen et al. 2014; Fu et al. 2018) as the training grid for the RF algorithm. The training grid comprises a grid of stellar parameters covering 7000 K $< T_{\rm eff} <$ 49 000 K, $0.55 < \log g < 4.52$ dex, and $-0.6 <$ [M/H] < 0.6 dex. The process begins with the prediction of luminosity using $T_{\rm eff}$, $\log g$ and [M/H]. This predicted luminosity, along with $T_{\rm eff}$, $\log g$ and

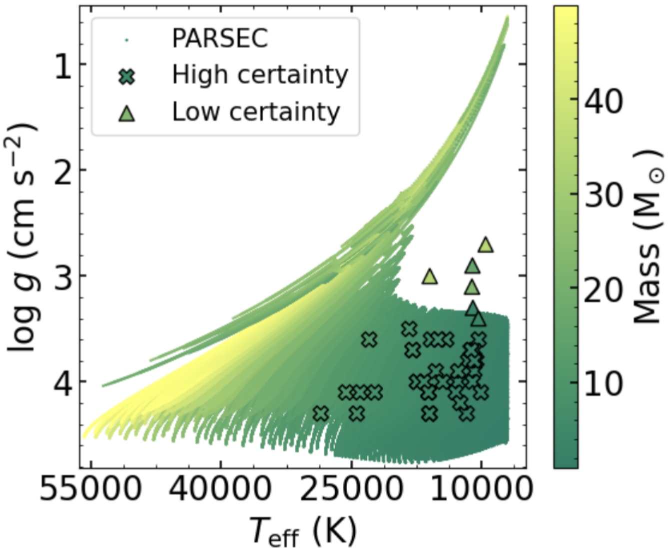

Fig. 3. Training grid and predicted sample in the log g–$T_{\rm eff}$ plane. The background shows the PARSEC 1.2S main-sequence grid color-coded by stellar mass. The black crosses and triangles represent our 45 B-type runaway stars, with colors corresponding to their predicted masses using the same color scale. Crosses denote stars within the parameter range of the training grid (high certainty), while triangles indicate extrapolated sources outside the grid (low certainty).

[M/H], is then used to predict stellar mass. Finally, the model predicts stellar age based on $T_{\rm eff}$, log g, [M/H], as well as the previously derived luminosity and mass. Validation of the method shows that the uncertainty of mass prediction is 9%, whereas the age dispersion is 0.44 Gyr. The larger dispersion in age prediction arises from poorly constrained metallicity in early-type stars and the inherent age–metallicity degeneracy.

The derived masses and ages are presented in Table A.1. Figure 3 illustrates the PARSEC1.2S training grid in the log g–$T_{\rm eff}$ plane, color-coded by stellar mass. Our predicted sources are overplotted as black symbols using the same mass color scale. Crosses mark stars located within the training grid ("high certainty"), whereas triangles correspond to extrapolated objects outside the grid ("low certainty"). These two cases are also flagged as "I" (inside) and "O" (outside) in Table A.1. From the figure, six stars are found to lie outside the training grid – one of them have $T_{\rm eff}$ and log g within the grid boundaries but fall outside in [M/H]. Since the RF model extrapolates for these out-of-range inputs, their predicted masses and ages are deemed unreliable, and sources marked with a triangle are also considered to lie outside the main-sequence phase. Four of these outliers exhibit unusually high inferred masses (>16 $M_\odot$), further supporting their exclusion. Therefore, we removed these six stars from the subsequent analysis, resulting in a final sample of 39 B-type runaway stars.

3.4. Orbital trajectories

Having derived the atmospheric and fundamental parameters, we used the Python package GALPY (Bovy 2015) to calculate the Galactic trajectories of our stars. Proper motions were retrieved from *Gaia* Early Data Release 3 (Gaia Collaboration 2021), and distances were obtained from the posterior distribution of geometric distances by Bailer-Jones et al. (2021), while radial velocities and peculiar space velocities ($V_{\rm Sp}$) were taken from Guo et al. (2024). We adopted the solar motion of ($U_\odot$,$V_\odot$,$W_\odot$) = (11.10, 12.24, 7.25) km s^{-1} from Schönrich et al. (2010) and both the solar Galactocentric distance (R_0) of 8.5 kpc and the circular Galactic rotational velocity (V_c) of 220 km s^{-1} from Kerr & Lynden-Bell (1986, see Guo et al. 2024). We determined the uncertainties in the birthplaces of the 39 stars by conducting Monte Carlo simulations, assuming Gaussian error distributions for distances, proper motions, radial velocities, and ages (Liu et al. 2023).

4. Results

4.1. Orbital trajectories of stars

Although the Milky Way's disk flare and warp cause the exponential scale-height to increase with Galactocentric radius, reported values vary among studies because they use different populations and methods (López-Corredoira & Molgó 2014; Wang et al. 2018a; Yu et al. 2021). Based on LAMOST DR5 OB stars, Yu et al. (2021) derived a scale-height increasing from 0.14 to 0.5 kpc over R = 8–14 kpc, similar to the thin disk values reported by Wang et al. (2018a). For the thick disk, López-Corredoira & Molgó (2014) and Wang et al. (2018b) reported scale-heights of 0.5–1.5 kpc over R = 8–20 kpc. Considering the different scale heights of the thin and thick disks, and the R distribution of our sample, we adopted $|Z|$ = 0.5 kpc[2] as the threshold to distinguish disk objects (Liu et al. 2023). Notably, there is no rigid border orthogonal to the Galactic disk, and in a disk population with a given scale height, about 30% of the stars may extend beyond that height.

After computing the Galactic orbits of our stars, we present the trajectories of four example stars in Figs. 4 and 5, shown in the Galactic $X-Y$ and $R-Z$ planes, with travel time defined as the elapsed time for a star to move from its birthplace to its current position. Figure 4 shows two examples of stars for which there is no significant change between their current locations and their birthplaces and their orbits remain confined within $|Z| < 0.5$ kpc, supporting a disk origin. In total, 29 stars exhibit this behavior. In the top panel of Fig. 5, although the trajectories pass through the disk, the birthplaces of stars can still be traced back to within $|Z| < 0.5$ kpc, and 9 stars in our sample fall into this category. Notably, we use the term "pass through the disk" (or "disk-passing") to describe stars whose orbits pass the Galactic disk region (defined here as being within $|Z| <= 0.5$ kpc), which can involve passing through and leaving the disk or possibly returning to it at a later time. In the bottom panel of Fig. 5, the birthplace of this star is closer to the disk edge, but after considering the Monte Carlo uncertainties, they can still be regarded as having a disk origin. We have one such source. In summary, 29 stars have trajectories entirely confined within the disk, while 10 stars have trajectories that pass through the disk but can still be considered to have a disk origin.

4.2. Possible cluster origin

To investigate potential DESs, we cross-matched our sample of 39 stars with cluster catalogs (Castro-Ginard et al. 2019, 2020; Hunt & Reffert 2023) and found that the trajectories of only two sources intersect with those of clusters. We also used the Python package GALPY (Bovy 2015) to calculate the Galactic trajecto-

---

[2] We also tested a smaller boundary of $|Z|$ = 0.14 kpc and found that, when considering the uncertainties in the birth positions, all of our stars still originate from within the Galactic disk.

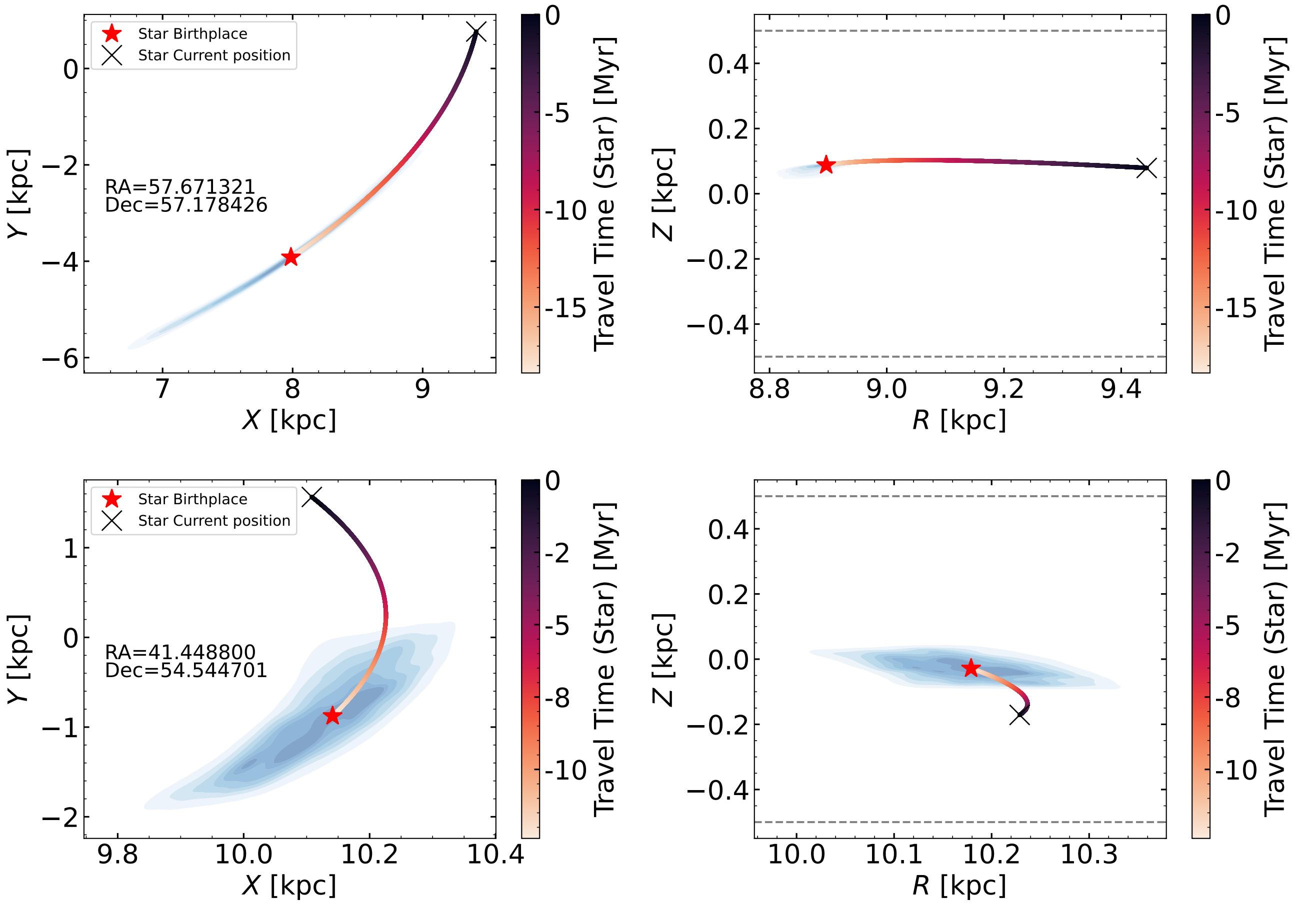

Fig. 4. Orbital trajectories for two example stars with coordinates RA: 57.671321, Dec: 57.178426 (top panels) and RA: 41.448800, Dec: 54.544701 (bottom panels), shown in the Galactic $X - Y$ plane (left panels) and the Galactic $R - Z$ plane (right panels). The color scale indicates travel time (in Myr), with the red star marking each star's birthplace and the black "x" marking its current position. The red-shaded contours denote the uncertainty regions of the birthplaces.

ries for the two matched clusters; we show the results in Figs. 6 and 7.

Figure 6 displays the orbital trajectories of a star with RA = 102.2630, Dec = 41.9814 and its matched cluster IC 1311. The star has $T_{\rm eff}$ = 10 339 K, log g = 3.65, and [M/H] = −0.48, while the metallicity of IC 1311 is [M/H] = −0.30 ± 0.16 as reported by Warren & Cole (2009). In the Galactic $X - Y$ plane, both the star and the cluster move counterclockwise, while in the $R - Z$ plane their trajectories broadly overlap. The similarity between their orbital trajectories and metallicities may suggest that the star originated from the cluster.

Figure 7 displays the orbital trajectories of a star with RA = 41.4488, Dec = 54.5447 and its matched cluster NGC 2236. The star has $T_{\rm eff}$ = 9890 K, log g = 3.87, and [M/H] = −0.28. The metallicity of NGC 2236 is [M/H] = −0.19 ± 0.08 as reported by Zhong et al. (2020). The orbital trajectories in Fig. 7 show that the star was initially close to NGC 2236, but later moved away from the cluster's orbit in the R–Z projection. This may suggest that the star was ejected from the cluster. Notably, definitive confirmation would require further evidence. As noted by Hoogerwerf et al. (2001), compelling evidence for the DES involves finding a common site of origin for the individual components of the encounter.

4.3. Statistical properties

Figure 8 presents the distribution of runaway stars in the $V_{\rm Sp} - \upsilon \sin i$ plane. It shows that the majority of B-type runaways lie in the gray region, corresponding to low peculiar space velocities and low $\upsilon \sin i$. The disk-confined subsample (black dots) has relatively low peculiar space velocities and spans a wide range of $\upsilon \sin i$, whereas the disk-passing subsample (red stars) tends to have higher $V_{\rm Sp}$ while maintaining low $\upsilon \sin i$. According to Sana et al. (2022), slow-moving, rapidly rotating runaways point to the BSS, while fast-moving, slowly rotating runaways are more consistent with the DES. Rapidly rotating runaway stars are interpreted as products of close binary interactions, such as stellar mergers (Podsiadlowski et al. 1992; Tylenda et al. 2011) or mass transfer (Packet 1981; Petrovic et al. 2005), which can significantly increase the rotational velocity (Sana et al. 2022). By contrast, the DES involves close multi-body encounters that impart large $V_{\rm Sp}$ without significantly spinning up the ejected stars (Sana et al. 2022). In addition, stars with a possible BSS origin tend to be disk-confined, whereas those with a possible DES origin are disk-passing. While our orbital traceback provides statistical support for these trends, more definitive conclusions will require high-resolution spectroscopic data in future work.

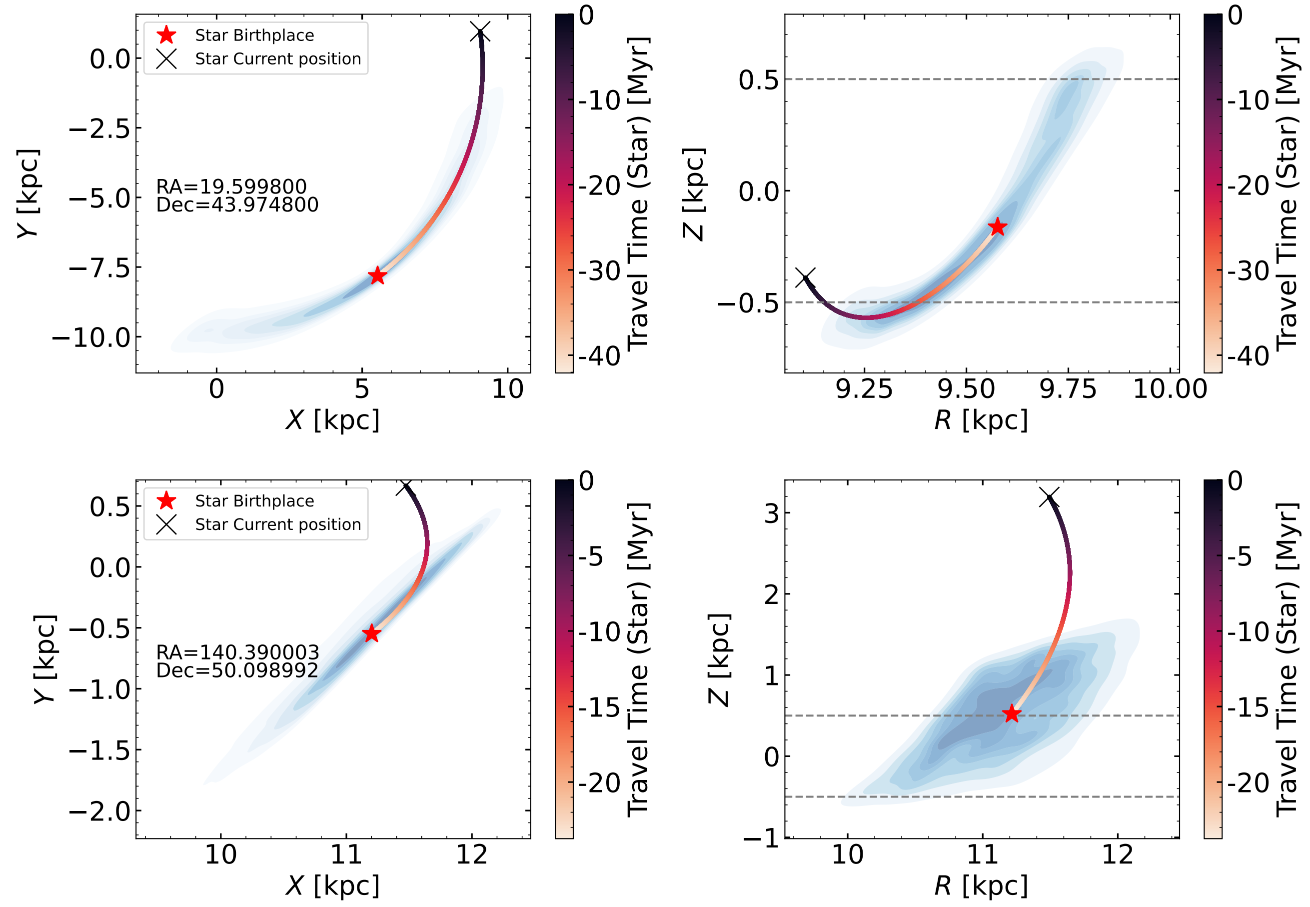

Fig. 5. Same as Fig. 4 but for stars with coordinates RA: 19.599800, Dec: 43.974800 (top panels) and RA: 140.390003, Dec: 50.098992 (bottom panels).

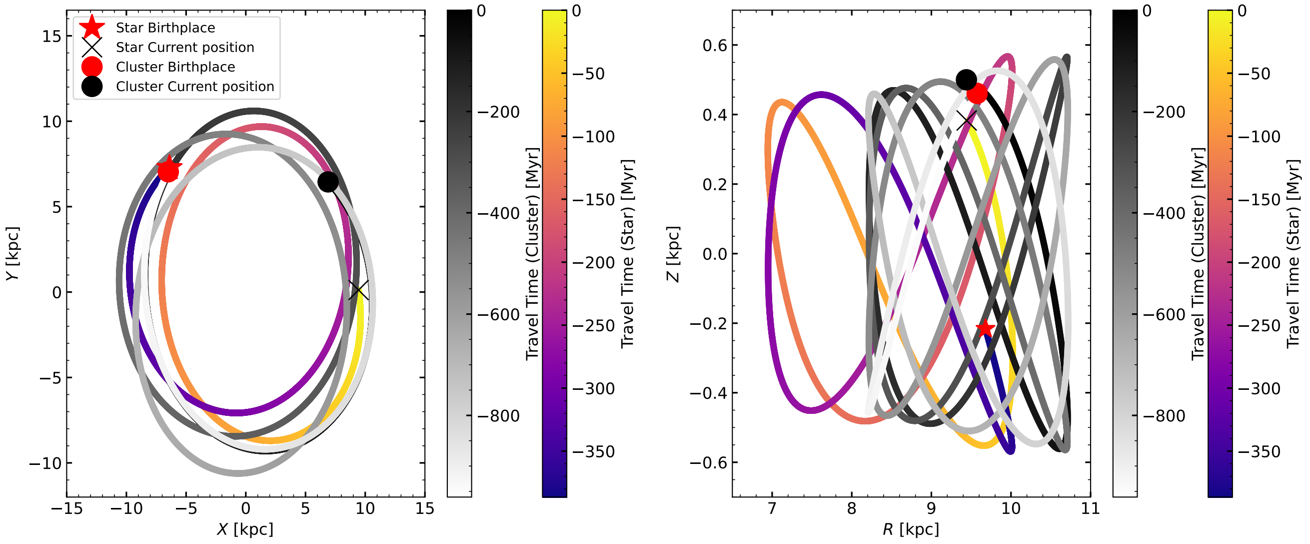

Fig. 6. Orbital trajectories of IC 1311 and its matched star (RA = 102.263087, Dec = 41.981471) in Galactic coordinates. We show the orbits of the star (colored by travel time in Myr) and the cluster (in grayscale) in the Galactic $X-Y$ (left) and Galactic $R-Z$ projections (right). The red star and red circle mark the birthplaces of the star and cluster, while the black cross and black circle indicate their current positions. The colorbars indicate the look-back time along each orbit, with negative values corresponding to earlier times.

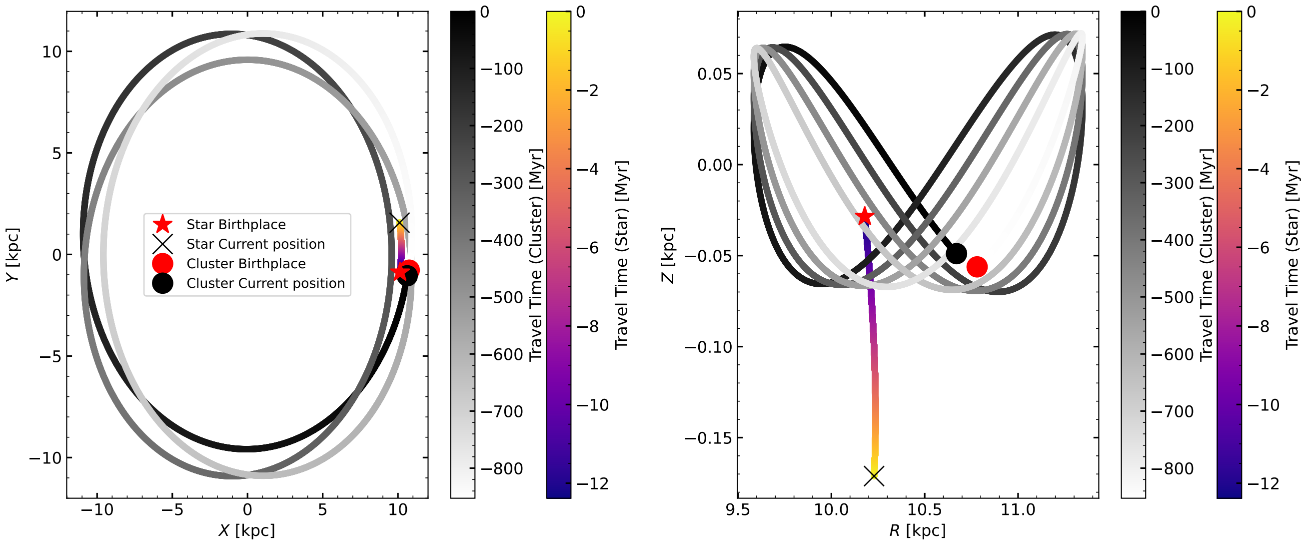

Fig. 7. Same as Fig. 6 but for NGC 2236 and its matched star (RA = 41.4488, Dec = 54.5447).

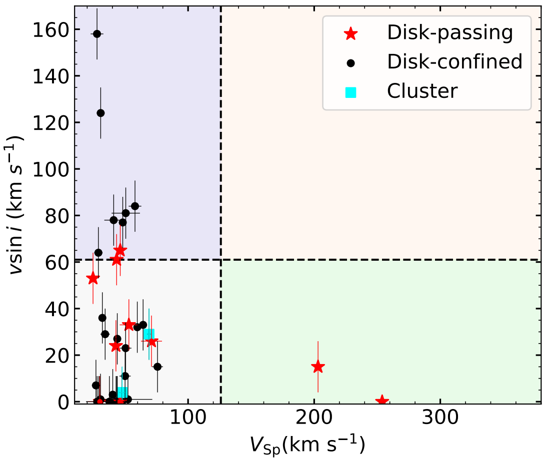

Fig. 8. Distribution of runaway stars in the $V_{Sp} - v \sin i$ plane. Stars with orbits remaining within the Galactic disk are marked as black dots, those with disk-passing orbits as red stars, and possible cluster-origin runaways as cyan squares. Thresholds of $v \sin i = 61\,\mathrm{km\,s^{-1}}$ and $V_{Sp} = 126\,\mathrm{km\,s^{-1}}$ (dashed lines) represent the 3σ values obtained from Maxwellian fits to the observed distributions, as described in Sect. 4.3 of Guo et al. (2024).

5. Summary

Runaway stars rapidly escape from their birth clusters or associations, typically with peculiar velocities of 30–40 km/s. Two mechanisms are typically considered, the BSS and the DES, but their relative contributions remain uncertain. Determining the origins of runaways may provide constraints on binary evolution and dynamical processes.

In this work we investigated the kinematic origins of 39 B-type runaway stars identified by Guo et al. (2024). We determined spectral subclasses from key absorption lines and derived atmospheric parameters with SLAM. We then estimated fundamental parameters using a machine learning model trained on these parameters. Using GALPY, we computed each star's Galactic trajectory: we find that 29 stars remain fully confined to the disk and 10 have disk-passing orbits yet still trace back to the disk. Two of these may be consistent with a cluster origin, although a definitive confirmation would require further evidence. We also find a feature in the $V_{Sp} - v \sin i$ plane: low-V_{Sp}, high-$v \sin i$ runaways are typically disk-confined, whereas high-V_{Sp}, low-$v \sin i$ runaways are disk-passing. This probably reflects two different origins. This may provide new kinematic evidence that can be used to distinguish between the BSS and the DES. However, our conclusions are limited by the lack of high-resolution spectroscopic abundances. Future surveys with higher-precision spectroscopy will be crucial to establishing firmer constraints on the origins of runaway stars and their role in binary evolution and cluster dynamics.

Acknowledgements. This work is supported by the National Natural Science Foundation of China (Nos. 12288102, 12125303, 12090040/3, 12103064, 12403039, 12373036), the National Key R&D Program of China (grant Nos. 2021YFA1600403/1, 2021YFA1600400), and the Natural Science Foundation of Yunnan Province (Nos. 202201BC070003, 202001AW070007), the International Centre of Supernovae, Yunnan Key Laboratory (No. 202302AN360001), the "Yunnan Revitalization Talent Support Program"-Science, Technology Champion Project (N0. 202305AB350003), and Yunnan Fundamental Research Projects (grant Nos. 202501CF070018). This work has been supported by the New Cornerstone Science Foundation through the XPLORER Prize.

References

Bailer-Jones, C. A. L., Rybizki, J., Fouesneau, M., Demleitner, M., & Andrae, R. 2021, AJ, 161, 147
Beers, T. C., Almeida, T., Rossi, S., Wilhelm, R., & Marsteller, B. 2007, ApJS, 168, 277
Berger, D. H., & Gies, D. R. 2001, ApJ, 555, 364
Blaauw, A. 1961, Bull. Astron. Inst. Netherlands, 15, 265
Blaauw, A., & Morgan, W. W. 1954, ApJ, 119, 625
Bovy, J. 2015, ApJS, 216, 29
Bressan, A., Marigo, P., Girardi, L., et al. 2012, MNRAS, 427, 127
Brown, W. R., Beers, T. C., Wilhelm, R., et al. 2008, AJ, 135, 564
Carretero-Castrillo, M., Ribó, M., & Paredes, J. M. 2023, A&A, 679, A109
Cassinelli, J. P., & Churchwell, E. B. 1993, Massive Stars: Their Lives in the Interstellar Medium, 35
Castro-Ginard, A., Jordi, C., Luri, X., Cantat-Gaudin, T., & Balaguer-Núñez, L. 2019, A&A, 627, A35
Castro-Ginard, A., Jordi, C., Luri, X., et al. 2020, A&A, 635, A45
Catelan, M. 2009, Ap&SS, 320, 261
Chen, Y., Girardi, L., Bressan, A., et al. 2014, MNRAS, 444, 2525

Chen, K., Guo, Y., Jiang, D., Han, Z., & Chen, X. 2025, ApJ, 988, 228
Cui, X.-Q., Zhao, Y.-H., Chu, Y.-Q., et al. 2012, Res. Astron. Astrophys., 12, 1197
Culpan, R., Pelisoli, I., & Geier, S. 2021, A&A, 654, A107
Deng, L.-C., Newberg, H. J., Liu, C., et al. 2012, Res. Astron. Astrophys., 12, 735
Fu, X., Bressan, A., Marigo, P., et al. 2018, MNRAS, 476, 496
Gaia Collaboration (Brown, A. G. A., et al.) 2021, A&A, 649, A1
Gies, D. R., & Bolton, C. T. 1986, ApJS, 61, 419
Gray, R. O., & Corbally, C. j. 2009, Stellar Spectral Classification (Princeton University Press)
Guo, Y., Zhang, B., Liu, C., et al. 2021, ApJS, 257, 54
Guo, Y., Wang, L., Liu, C., et al. 2024, ApJS, 272, 45
Guo, Y., Chen, K., Li, Z., et al. 2025, A&A, 702, A11
Herbig, G. H. 1995, ARA&A, 33, 19
Hoffer, J. B. 1983, AJ, 88, 1420
Hoogerwerf, R., de Bruijne, J. H. J., & de Zeeuw, P. T. 2000, ApJ, 544, L133
Hoogerwerf, R., de Bruijne, J. H. J., & de Zeeuw, P. T. 2001, A&A, 365, 49
Hunt, E. L., & Reffert, S. 2023, A&A, 673, A114
Irrgang, A., Przybilla, N., Heber, U., Nieva, M. F., & Schuh, S. 2010, ApJ, 711, 138
Ju, J., Cui, W., Huo, Z., et al. 2024, ApJS, 270, 11
Kerr, F. J., & Lynden-Bell, D. 1986, MNRAS, 221, 1023
Lanz, T., & Hubeny, I. 2007, ApJS, 169, 83
Li, Q., Xiong, J., Li, J., et al. 2025, ApJS, 276, 19
Liu, Z., Cui, W., Liu, C., et al. 2019, ApJS, 241, 32
Liu, C., Fu, J., Shi, J., et al. 2020, ArXiv e-prints [arXiv:`2005.07210`]
Liu, Z., Cui, W., Zhao, G., et al. 2023, MNRAS, 519, 995
López-Corredoira, M., & Molgó, J. 2014, A&A, 567, A106
Maíz Apellániz, J., Pantaleoni González, M., Barbá, R. H., et al. 2018, A&A, 616, A149
McEvoy, C. M., Dufton, P. L., Smoker, J. V., et al. 2017, ApJ, 842, 32
Mdzinarishvili, T. G., & Chargeishvili, K. B. 2005, A&A, 431, L1
Packet, W. 1981, A&A, 102, 17
Petrovic, J., Langer, N., & van der Hucht, K. A. 2005, A&A, 435, 1013
Podsiadlowski, P., Joss, P. C., & Hsu, J. J. L. 1992, ApJ, 391, 246
Poveda, A., Ruiz, J., & Allen, C. 1967, Boletin de los Observatorios Tonantzintla y Tacubaya, 4, 86
Przybilla, N., Fernanda Nieva, M., Heber, U., & Butler, K. 2008, ApJ, 684, L103
Renzo, M., Zapartas, E., de Mink, S. E., et al. 2019, A&A, 624, A66
Salgado, C., Moni Bidin, C., Villanova, S., Geisler, D., & Catelan, M. 2013, A&A, 559, A101
Sana, H., Ramírez-Agudelo, O. H., Hénault-Brunet, V., et al. 2022, A&A, 668, L5
Schönrich, R., Binney, J., & Dehnen, W. 2010, MNRAS, 403, 1829
Stone, R. C. 1979, ApJ, 232, 520
Teklehaimanot, B. T., & Gebrehiwot, Y. M. 2024, New Astron., 106, 102128
Tylenda, R., Hajduk, M., Kamiński, T., et al. 2011, A&A, 528, A114
van den Heuvel, E. P. J., Portegies Zwart, S. F., Bhattacharya, D., & Kaper, L. 2000, A&A, 364, 563
Vickers, J. J., Li, Z.-Y., Smith, M. C., & Shen, J. 2021, ApJ, 912, 32
Wang, H., López-Corredoira, M., Carlin, J. L., & Deng, L. 2018a, MNRAS, 477, 2858
Wang, H.-F., Liu, C., Xu, Y., Wan, J.-C., & Deng, L. 2018b, MNRAS, 478, 3367
Wang, L., Li, J., Wu, Y., et al. 2022, ApJS, 260, 35
Warren, S. R., & Cole, A. A. 2009, MNRAS, 393, 272
Xiang, M., Rix, H.-W., Ting, Y.-S., et al. 2022, A&A, 662, A66
Xue, X. X., Rix, H. W., Zhao, G., et al. 2008, ApJ, 684, 1143
Yu, Y., Wang, H.-F., Cui, W.-Y., et al. 2021, ApJ, 922, 80
Zhang, B., Liu, C., & Deng, L.-C. 2020, ApJS, 246, 9
Zhao, G., Zhao, Y.-H., Chu, Y.-Q., Jing, Y.-P., & Deng, L.-C. 2012, Res. Astron. Astrophys., 12, 723
Zhong, J., Chen, L., Wu, D., et al. 2020, A&A, 640, A127
Zwicky, F. 1957, Morphological Astronomy (Springer)

Appendix A: Table

Table A.1. The predicted parameters of B-type runaway stars.

Gaia DR3 ID	Name	RA (deg)	DEC (deg)	Para (mas)	μ_α (mas yr^{-1})	μ_β (mas yr^{-1})	$T_{\rm eff}$ (K)	$\log g$ (dex)	$[M/H]$ (dex)	$v\sin i$ (km s^{-1})	Mass (M$_\odot$)	Age (Myr)	V_{Sp} (km s^{-1})	X (kpc)	Y (kpc)	Z (kpc)	U (km s^{-1})	V (km s^{-1})	W (km s^{-1})	Class	Flag
454303606011095552	LS V+545	41.4488	54.5447	0.3927	0.803	-2.306	25621	4.1	–0.2	29	10.0	12.4	34.24	10.19	1.66	0.23	11.32	194.09	-14.63	B2	I
160785506636872064	HD 282581	74.1620	32.9081	0.733	1.555	-6.167	15841	3.6	–0.8	158	5.3	78.1	27.8	9.61	0.22	0.17	4.78	192.62	3.64	B5	I
3443256628164281216		87.9204	28.9357	0.285	1.952	-2.237	16643	4.0	–0.5	78	4.8	79.2	41.01	11.78	-0.04	0.09	-40.07	241.19	10.33	B5	I
3326494643686889088	TYC 733-1378-1	99.5149	8.6713	0.6573	-1.109	2.748	14466	4.0	–1.3	0	3.1	271.3	29.29	9.66	-0.61	0.05	-8.21	216.6	-18.13	B7	I
3326494643686889088	LS VI +00 39	106.4899	0.4331	0.1677	0.57	0.564	18337	3.5	–0.5	0	8	36.1	46.17	13.19	-3.35	0.38	-68.24	186.58	34.37	B2-4	I
413562439598069504	TYC 3677-432-1	16.9278	57.2203	0.3471	-2.547	-1.52	17439	4.0	-0.6	23	4.8	77.6	50.49	9.92	2.34	0.30	87.44	181.81	-7.46	B3	I
397517678722323328	HD 7800	19.5998	43.9747	0.7517	-2.109	1.559	16010	4.3	-0.3	53	4.1	42.1	24.63	9.05	0.99	0.45	-6.5	197.06	-10.94	B6	I
398938724484157696	HD 8853	22.0482	46.4773	0.7883	-2.284	4.316	10862	3.7	-0.9	61	2.7	436.1	43.33	9.05	0.94	0.37	40.83	223.56	39.14	B9	I
408242658738755072	TYC 3684-1905-1	27.9584	53.8468	0.2492	-0.588	-1.717	24381	4.3	-0.3	0	8.2	9.2	30.08	10.92	2.96	0.58	-1.37	182.3	5.81	B2	I
504636499555620608	TYC 3688-855-1	29.52	55.8277	0.2252	-0.643	-0.919	23994	4.1	-0.3	1	9.0	16.0	52.32	11.24	3.27	0.47	17.41	237.37	-14.99	B2-4	I
439486484232540032		43.8182	49.9802	0.6798	0.159	-5.119	16119	4.1	-0.5	0	4.0	111.5	42.9	9.42	0.89	0.23	37.96	228.0	-10.86	B5	I
243078420061155200	Cl Melotte 20 616	51.1356	47.0336	1.1389	-0.068	-2.526	11558	3.8	-0.5	84	2.8	331.7	57.91	9.01	0.46	0.15	62.21	193.91	7.43	B8	I
469854136404332160	BD+56 849	57.6713	57.1784	0.7153	-0.721	-2.025	22302	4.1	-0.3	11	7.6	18.4	50.04	9.42	0.79	0.08	-21.8	249.21	-4.7	B2-4	I
3312653956955249024	HD 28868	68.3573	15.9609	0.8905	-3.1	-14.988	28530	4.3	-0.7	15	11.0	6.0	75.77	9.32	-0.02	0.42	43.29	180.31	-47.48	B3	I
204537818788471552		72.4418	43.3329	0.5487	-0.405	-3.05	10840	3.9	-0.3	33	2.7	398.5	64.34	10.00	0.57	0.05	70.1	193.89	-11.32	B9V	I
3418315443837401856	TYC 1845-611-1	75.838	22.709	0.2978	0.305	-2.314	11111	3.1	-0.5	1	23.0	7.1	24.98	11.56	0.01	0.68	-14.95	191.6	-5.79	B8	O
182839751387484544	TYC 2411-858-1	81.4654	34.645	0.6078	-0.906	2.362	16119	4.1	-0.5	3	4.0	111.5	40.27	9.90	0.20	0.03	-30.03	191.4	9.95	B7	I
3448992810388646272		82.1411	32.7145	0.4042	0.575	-3.261	16119	4.1	-0.5	7	4.0	111.5	26.94	10.73	0.22	0.07	21.78	197.4	1.21	B6	I
183095216044126464		82.905	35.4471	0.2505	0.923	-1.944	14069	3.6	0.2	0	5.0	93.5	27.92	12.23	0.49	0.09	13.41	195.91	-1.94	B7	I
182971520985243264	LS V +34 50	83.2549	34.6184	0.3639	0.084	-1.044	17946	3.7	-0.5	29	5.8	67.9	69.05	11.00	0.30	0.06	-62.68	228.23	1.73	B3	I
3217785516730554496	TYC 4766-2044-1	84.0704	-0.3599	0.8261	5.409	-2.249	11265	3.7	-0.6	36	3.0	305.0	32.03	9.32	-0.48	0.37	7.28	197.98	1.9	B8	I
190927930719003776	TYC 2914-560-1	84.1875	39.611	0.8708	-0.451	-2.443	17439	4.0	-0.6	77	4.8	77.6	48.2	9.40	0.20	0.10	52.23	214.88	-5.06	B3IV-V	I
191721670736788992		86.812	39.9896	0.5017	4.061	-1.648	11024	4.0	-0.8	24	2.4	463.0	42.79	10.23	0.32	0.23	-7.79	246.0	26.3	B9.5	I
3443887369881254912		88.0811	29.8264	0.3751	0.757	-3.157	15278	3.9	-0.6	0	4.0	130.7	29.26	10.93	0.00	0.10	9.91	245.71	6.8	B6	I
3424904026749213184	V* EO Tau	90.0723	23.9107	0.3761	-0.957	-2.09	16010	4.3	-0.3	0	4.1	55.0	47.7	10.91	-0.28	0.03	-49.05	208.96	-16.01	B8	I
3429641341319637632	TYC 1868-1977-1	90.9519	25.5211	0.5029	1.831	-4.282	12734	4.0	-0.6	4	3.0	257.2	47.73	10.25	-0.17	0.08	-35.2	184.39	4.02	B8	I
3430580560467553280	TYC 1876-1681-1	91.0773	28.2141	0.2269	0.387	-2.001	16010	4.3	-0.3	1	4.1	55.0	30.55	12.67	-0.21	0.26	-10.02	229.94	-16.91	B8.5	I
3453566198941548160		91.6201	35.9211	0.807	-0.298	-8.571	10609	3.8	-1.3	81	2.0	817.4	50.59	9.50	0.08	0.18	33.66	187.14	-21.68	B8	I
3426385721747313920	TYC 1868-2918-1	91.9593	25.0776	0.267	0.504	-2.747	16119	4.1	-0.5	0	4.0	111.5	37.61	11.99	-0.38	0.17	65.56	198.13	-1.53	B7	I
3007731791705065088	TYC 4796-1084-1	94.1485	-6.7794	0.6563	-0.777	-2.549	11002	3.3	-0.6	13	4.0	164.0	28.32	9.50	-0.86	0.31	4.2	226.78	-10.07	B9	O
3433498011492658432		95.8672	28.0711	0.3432	0.06	-1.418	12704	3.9	0.3	0	4.0	114.4	43.23	11.15	-0.24	0.37	-46.22	209.53	6.06	B8	I
3386487227913057792	TYC 1905-733-1	100.9098	28.6649	1.3093	26.315	-21.228	10848	3.8	-1.0	15	2.1	693.5	203.07	9.02	-0.08	0.17	182.35	140.45	30.78	B9	I
951827356237232256	TYC 2949-1606-1	102.2387	42.1852	0.682	0.791	-4.915	15017	3.6	0.3	0	5.7	57.5	43.87	9.66	0.15	0.46	38.19	195.29	-9.97	B5	I
951731050186706432	TYC 2949-616-1	102.2631	41.9815	0.7602	5.446	-4.093	10339	3.6	-0.5	33	2.8	386.5	53.06	9.52	0.13	0.41	44.07	192.55	19.23	B9	I
3111724013778184832	HD 289860	108.8516	0.789	0.4931	-3.729	1.997	17946	3.7	-0.5	124	6.2	56.2	30.71	9.92	-1.16	0.22	31.17	232.66	9.36	B4	I
879741935106643200	TYC 2453-1455-1	113.2647	30.4244	0.5595	0.321	-1.286	11194	3.7	-0.4	65	3.0	324.7	46.22	9.91	-0.25	0.68	40.1	225.43	-4.91	B9	I
874101715335862656	TYC 1933-1771-1	117.6444	26.3668	1.8169	4.691	-32.421	11057	2.9	0.7	10	16.3	7.2	76.86	8.76	-0.12	0.24	26.8	149.78	-8.97	B9	O
3098381234015269248	TYC 794-327-1	124.1998	8.9158	0.4447	-2.181	2.439	15971	3.0	-0.8	0	34.6	5.0	55.99	9.97	-1.17	0.90	-72.74	215.21	30.19	B2	O
1018951342817806976	HD 233622	140.39	50.099	0.1759	3.469	-9.056	22948	3.6	-1.0	0	10.0	23.7	253.91	12.26	0.84	3.99	45.79	-4.2	114.19	B2-4	I
1280720146285434752	Feige 98	219.5657	27.4925	0.5067	-10.344	-9.1	10369	3.4	-1.4	15	3.4	267.0	116.26	7.66	0.51	1.83	18.55	116.04	70.02	B9V	O
2078139584242969088		294.3707	42.9261	0.4107	-2.997	-10.45	11710	4.3	-0.8	26	2.1	425.6	70.99	7.69	2.32	0.46	131.74	207.94	-17.28	B9	I
2080113860450356352	TYC 3557-2105-1	297.0208	45.3604	1.6185	10.124	13.971	10083	4.1	-0.4	32	2.2	543.1	59.73	8.16	0.60	0.13	-37.18	246.79	1.84	B9	I
1982340682299842944	HD 215565	341.3406	44.8593	1.3478	-8.003	-3.114	9533	2.7	-0.1	24	34.7	4.8	29.25	8.40	0.71	0.18	2.4	217.92	7.73	B9	O
1935787909736139648	V* VY Lac	342.4964	45.0044	1.0298	5.447	-6.016	12991	4.1	-0.9	27	2.4	409.6	43.86	8.46	0.93	0.23	11.81	180.94	-18.4	B8	I
1999048002009372160	TYC 4009-521-1	356.7672	57.7945	0.9789	-5.473	-1.165	12449	4.2	0.2	64	3.2	111.4	28.89	8.69	0.93	0.09	-13.77	217.45	32.77	B8	I